



## Effect of phase transition on room temperature ferromagnetism in cerium doped ZnS nanorods

Nachimuthu SUGANTHI, Kuppusamy PUSHPANATHAN

Nanomaterials Research Laboratory, Department of Physics, Government Arts College, Karur-639 005, India

Received 9 April 2018; accepted 13 August 2018

**Abstract:** The effects of Ce doping on the structure, optical, oxidation, thermal and magnetic properties of ZnS:Ce nanorods synthesized by a chemical co-precipitation method were reported. The crystalline phase transformation from cubic to hexagonal structure was observed upon doping ZnS with Ce. Magnetic measurements showed the existence of room temperature ferromagnetism in Ce-doped ZnS nanorods. X-ray photoelectron spectroscopic (XPS) measurements provided evidence for Zn—S bonds and oxidation state of Ce in the near-surface region. Raman spectrum provided evidence for the presence of defects as well as hexagonal structure of 5 wt.% Ce doped ZnS nanorods. Ce substitution induced shape evolution was studied by using TEM. DRS spectra further validated the incorporation of Ce<sup>3+</sup> ions. The present study reveals that Ce doped ZnS nanorods may find applications in spintronic devices.

**Key words:** Ce dopant; ZnS nanorods; phase transition; ferromagnetism; sulphur vacancy; thermal stability

### 1 Introduction

Nanotechnology has provided a systematic pathway for investigating novel materials in the nanoscale range. Ferromagnetism in semiconductors at room temperature is a significant property of interest by virtue of their easy incorporation into semiconductor devices. Recently, rapid advancement in ferromagnetism is important for applications in physical, chemical, biological, electronic science and engineering sectors. ZnS is the only expected phase under ambient pressure conditions [1].

Recently, ZnS based d<sup>0</sup> ferromagnetism (FM) has been paid little attention to the experimental rather than the theoretical research. This magnetic property can be strongly determined by the defects in materials and not by the presence of magnetic ions [2,3]. Based on the fabrication methods, the defects (sulphur (or) zinc) existing in ZnS nanostructures have been reported [4,5]. d<sup>0</sup> ferromagnetism tuned by sulphur deficiency in ZnS nanoparticles of sphalerite structure grown by hydrothermal method [2] and wurtzite ultrathin ZnS NWs with zinc vacancies [6] has been studied. These S vacancies efficiently extend absorption spectra of ZnS to visible region [7]. Recently, the existence of low temperature and room temperature d<sup>0</sup> nano-ferromagnetism due to Zn vacancies in ZnS nanocrystals

has been reported based on experimental and theoretical standpoint [8].

Zinc sulphide nanocrystals can be efficient in nanospintronics [9] and they may become a novel class of emissive materials [10]. Magnetic properties of ZnS NPs without doping transition-metal atoms can possess some ultra-advantages for biomedical applications along with device applications. The absence of transition metal atoms may prevent the formation of dangerous free radical [6]. The ferromagnetism of the semiconductor NPs including doping with transition metal atoms or intrinsic ferromagnetism is especially interesting because it joins both the features of semiconductors and magnetic materials into a single nanoparticle. The exchange properties between the spin of the dopant atoms and the carriers in the semiconductor host give ferromagnetic order. However, transition metal doping in diluted magnetic semiconductors (DMS) leads to some problems of secondary phase and the mechanism of ferromagnetism is still unclear [11]. The angular momentum and the magnetic moment of a trivalent rare earth ion are entirely determined by the structure of the 4f shell. It has been established that the electrons in this shell couple their orbital and spin angular momenta together according to the Russell Saunders LS-coupling scheme [12]. Then, *L* and *S* couple into total angular momentum *J* by spin-orbit coupling. For a free ion, *J<sub>z</sub>* is

a constant of motion of the dynamic system. In a metal the crystalline field splits into levels of different  $J_z$ . In the first order theory the ions are usually treated as free. The crystalline field splitting may give rise to magnetic anisotropy [13].

Several studies on ZnS nanorods have been reported such as Green and one-step synthesis of ZnS nanorods in PEG 400 [14], chrome doped ZnS nanorods prepared by hydrothermal method [15,16], etc. Rare-earth doped wide-bandgap semiconductors have attracted considerable attention in recent years because of attempts to develop novel optoelectronic and spintronic devices. Recently, room-temperature ferromagnetism was studied in ZnS nanoparticles doped with RE elements like Nd [17],  $\text{Eu}^{3+}$  [18], Gd [19] and Ce doped ZnO [20]. 4f rare earth metals doped ZnS diluted magnetic semiconductor may offer stronger magnetism and anisotropy compared to transition metals with open d shells. Several rare-earth ions have large number of unpaired electrons and thus they provide high magnetic moments under a magnetic field. The crystal field plays an important role in influencing magnetic features of lanthanide ions [21]. In this circumstance, lanthanide ions exist in the weak field scheme, rather than transition metals. In lanthanide, the crystal field is small in comparison to spin-orbit interactions whereas the transition metal crystal field is larger compared to spin-orbit interactions. Doping with rare earth elements like cerium reduces the particle size of nanomaterials and it increases the surface area. It is proposed that magnetic  $\text{Ce}^{3+}$  ions introduced into nanoparticles of weak ferromagnetic system give rise to strong ferromagnetism.

In this study, Ce doped ZnS nanoparticles were synthesized and the structural, optical, magnetic and thermal properties were studied. Our experimental results suggest that the phase transition in the Ce doped sample may be responsible for the observed ferromagnetic behaviour.

## 2 Experimental

Commercial zinc sulphate, cerium (III) acetate and sodium sulphide were used as the sources of Zn, Ce and S, respectively. All the chemicals were used without further purification. In a typical procedure, appropriate amount of aqueous solutions of  $\text{ZnSO}_4 \cdot 7\text{H}_2\text{O}$ ,  $\text{C}_6\text{H}_9\text{CeO}_6 \cdot x\text{H}_2\text{O}$  and  $\text{Na}_2\text{S}$  were added together and stirred at 80 °C. PEG was also added with the aqueous solution. The resulting solution was stirred several hours. The as-prepared product was washed with distilled water and ethanol several times and then dried at room temperature. The obtained powders were annealed at 400 °C for 2 h under air atmosphere.

Thermal analysis was executed by thermo-

gravimetry differential scanning calorimetry (NETZSCH STA 449F3). Structural analysis was performed through Philips analytical X-ray diffractometer (Model No. PW 1830) using Cu  $K_\alpha$  radiation ( $\lambda=0.154187$  nm) over the broad range of diffraction angle  $2\theta=20^\circ\text{--}80^\circ$  at room temperature. X-ray photoelectron spectroscopy (XPS) measurement was performed using Thermo Scientific, MULTILAB 2000 base system with X-ray, Auger and ISS attachments. Twin anode Mg/Al (300/400W) was used as X-ray source. Diffuse reflectance spectra of the powders were recorded by using (Perkin Elmer-Lambda 35) Spectro photometer in the wavelength range of 200–800 nm. The morphology of ZnS and Ce doped ZnS was examined by transmission electron microscope (TEM: JEOL JEM 2010) operated at 200 kV accelerating voltage. The elemental composition of the synthesized materials was carried out by using EDS (JSM.6701\*F, Japan). The magnetic hysteresis ( $M\text{--}H$ ) loops were measured using vibrating sample magnetometer (Lakeshore–7400).

## 3 Results and discussion

### 3.1 Thermal studies

TG–DSC was used to study the crystallization temperature, phase transition, thermal decomposition and oxidation of as-synthesized and Ce doped ZnS nanorods and the results are presented in Fig. 1. The specimens were heated from room temperature upto 1200 °C at a step of 10 °C/min in nitrogen. Curve (1) depicts the TG of undoped ZnS and ZnS:Ce nanoparticles. For undoped ZnS there is a slight increase of mass at 28.7 °C. Owing to strong water absorption of ZnS, it adsorbs water from oxygen. There are three obvious mass loss regions up to 1200 °C in both undoped and Ce doped ZnS. The first mass loss of 3.53% is observed between the 0 and 343 °C for undoped ZnS, 2.7% is obtained from 343 to 305 °C for 5 wt.% Ce doped ZnS nanorods, due to the evaporation of water molecules. The degradation of sulphuric acid group causes the second mass loss of 1.3% at 687 °C for undoped ZnS and 3.46% at 804 °C for 5 wt.% Ce doped ZnS [22]. In addition to the mass loss observed up to 1200 °C, it is found that ZnS is oxidized into ZnO [23].

Curve (1) in Figs. 1(a) and (b) shows the DSC analysis of undoped and 5 wt.% Ce doped ZnS nanorods. The decomposition proceeds in two steps. First, an endothermic peak is observed at 202 °C for undoped ZnS. This is attributed to the removal of physically and chemically adsorbed water [24]. However, the peak observed at 203 °C for 5 wt.% Ce doped ZnS represents exothermic peak. The second peaks observed at 607 °C for undoped ZnS and at 624 °C for 5 wt.% Ce doped ZnS

nanorods show a broad exothermic peak, which is caused by the crystallization of ZnS. This implies the improvement of the crystallinity in the doped sample. Along with 630 °C, there is a smooth downward trend in the DSC curve with a significant mass loss. This might be due to the release of residual sulfur ions from the sample [25]. As the temperature further increases from 1000 to 1200 °C, the sample eventually suffers from oxidation. It is observed that the thermal stability of Ce doped sample is higher than that of the undoped ZnS. Based on the results, it may be concluded that the calcination temperature of 400 °C is sufficient to

crystallize the undoped and 5 wt.% Ce doped ZnS.

### 3.2 Microstructural and compositional analysis

Typical TEM images of undoped and 5 wt.% Ce doped ZnS are shown in Fig. 2. Figure 2(a) clearly reveals the spherical nanoparticle of undoped ZnS and the size of the nanoparticles estimated to be in the range 20–35 nm. Figures 2(b) and (c) show the representative TEM images of 5 wt.% Ce doped ZnS nanorods which are composed of spherical and rod like shape. TEM image is further used to obtain the  $d$  spacing values as shown in the inset of Fig. 2(b).

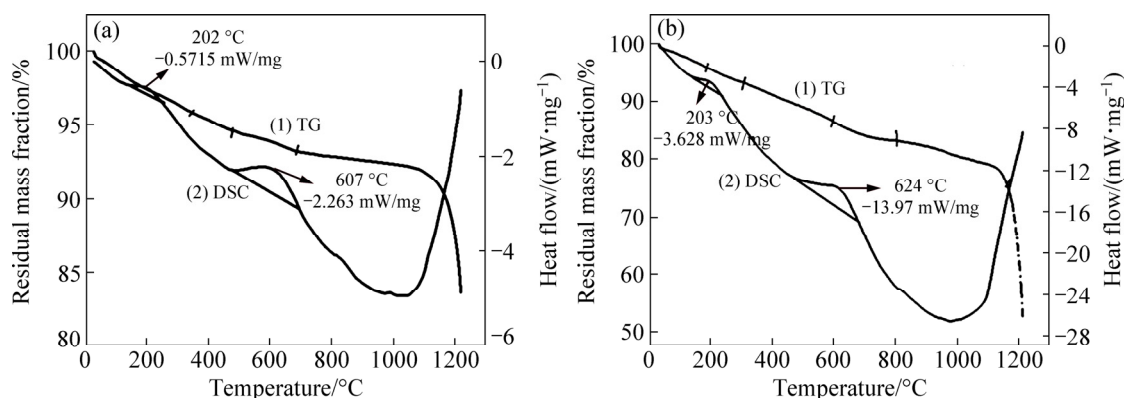


Fig. 1 TG and DSC curves of ZnS (a) and ZnS:Ce (5 wt.%) (b) nanorods

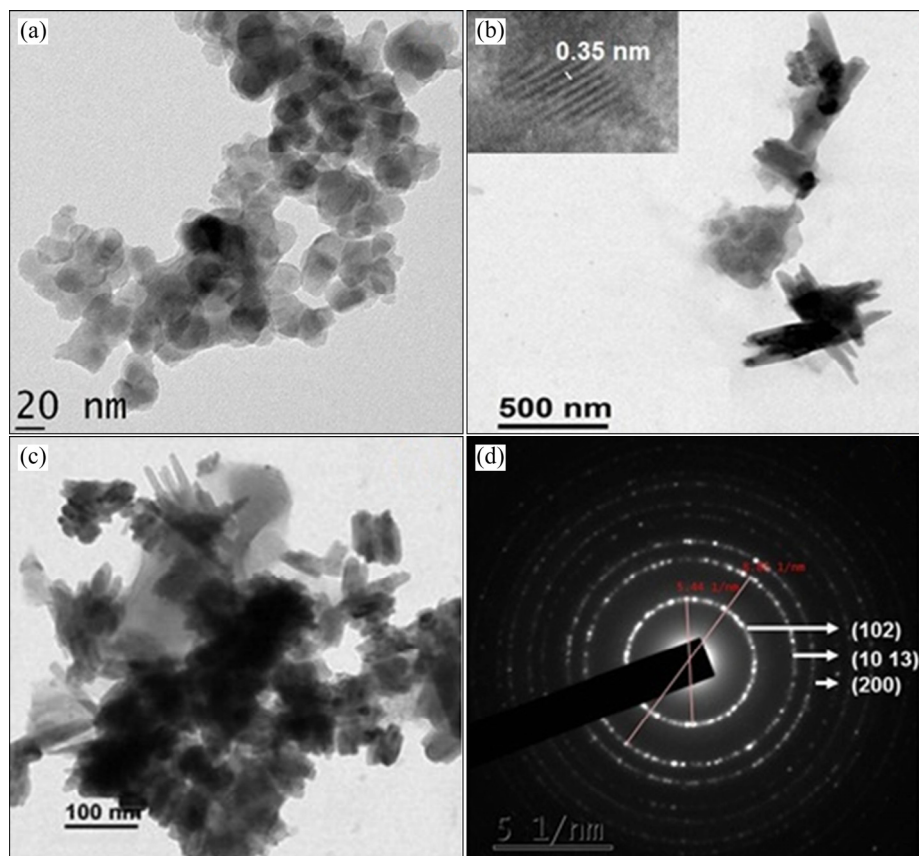


Fig. 2 Undoped ZnS (a), low (b) and high (c) magnification TEM images of 5 wt.% Ce doped ZnS nanorods and their corresponding SAED pattern (d)

The presence of clear lattice signifies the good crystallinity of the sample and the calculated lattice spacing (0.35 nm) corresponds to (102) plane of hexagonal phase of ZnS. This result confirms formation of crystalline nanorods. The polycrystalline nature of the sample is validated by SAED pattern (Fig. 2(d)) presenting a set of rings found as diffraction from different sets of planes of hexagonal ZnS. Figure 3 shows the EDAX spectrum which confirms the existence of Ce in the Ce doped ZnS nanorods. The detailed elemental composition in mole fraction is given in the inset of Fig. 3.

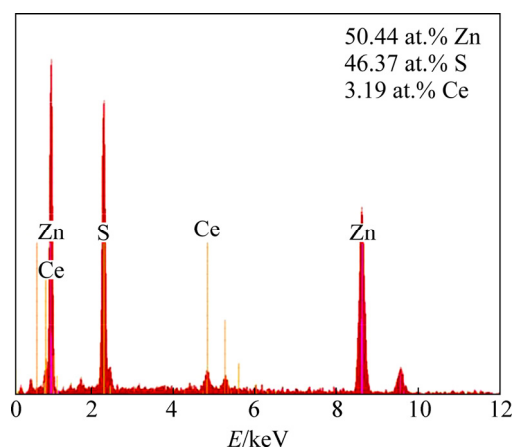


Fig. 3 EDAX spectrum of 5 wt.% Ce doped ZnS nanorods

### 3.3 Structural analysis

XRD spectra of ZnS and Ce doped ZnS are shown in Fig. 4(a). It is seen that the undoped ZnS nanoparticles exhibit three distinct peaks associated to cubic phase of ZnS as per JCPDS No. 65–5476. But the diffraction peaks of Ce doped sample are shifted to lower angle and the peaks observed at  $2\theta=27.5^\circ$ ,  $46.5^\circ$  and  $55.4^\circ$  match to the hexagonal phase. These diffraction peaks can be indexed as (102), (1013) and (200) which are in agreement with JCPDS File No. 89–2158. No impurity peaks are seen in both cubic and hexagonal phases indicating the high purity of the synthesized samples. The results suggest that  $Ce^{3+}$  is successfully incorporated into the ZnS host structure at the  $Zn^{2+}$  site. This is indeed interesting because the XRD pattern shows a structural transformation from cubic to hexagonal upon Ce doping

at room temperature. Furthermore, it can be observed that the peak intensity of Ce doped sample increases with doping concentration. High diffraction is an indication of more structural ordering, crystallization and arrangement.

The crystallite size and strain of the samples are calculated by Williamson and Hall plots by using profile fitting [26], as shown in Figs. 4 (b, c, d). The strains of the synthesized samples are found to be 0.00701,  $-0.012565$  and  $-0.091693$  for 0, 3 and 5 wt.% Ce, respectively. Here, negative sign indicates compressive strain in ZnS:Ce and this type of negative strain has been observed in Mn doped ZnS nanoparticles [27]. The

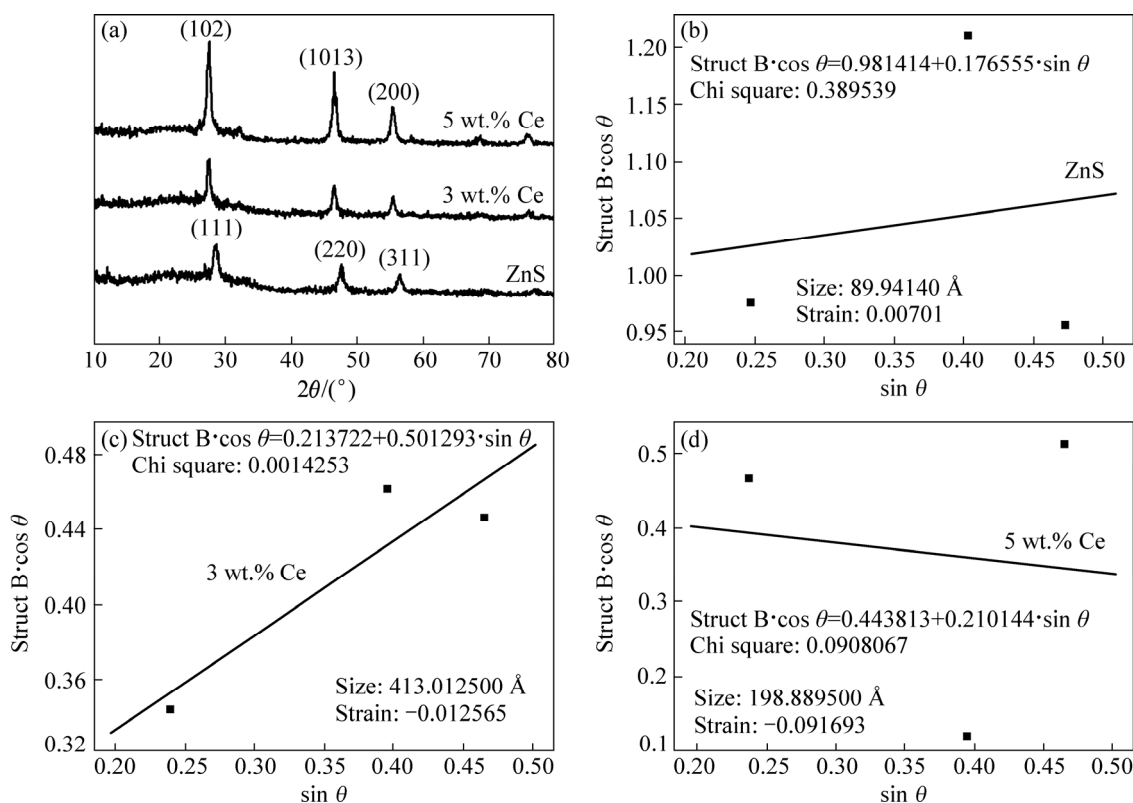


Fig. 4 XRD patterns and their corresponding Williamson and Hall plots by using profile fitting

crystallite sizes of ZnS and Ce doped ZnS (3 and 5 wt.% Ce) are estimated to be 8.8, 41.3 and 19.7 nm respectively. The lattice constants  $a$  and  $c$  have been determined from interplanar spacing of different ( $h k l$ ) planes, as shown in Table 1.

**Table 1** Comparison of crystallite size and strain from Williamson–Hall plots with lattice constants

Content of Ce/wt.%	Structure	Crystallite size/nm	Strain	Lattice parameter
0	Cubic	8.9	0.00701	$a=5.590$ nm
3	Hexagonal	41.3	-0.012565	$a=3.817$ nm, $c=31.19$ nm
5	Hexagonal	19.8	-0.091693	$a=3.831$ nm, $c=31.30$ nm

### 3.4 Oxidation state analysis

To study the compositions and the valence state of the annealed ZnS and Ce doped ZnS compound, X-ray photoelectron spectroscopy (XPS) analysis was carried out and the typical results are shown in Fig. 5. The full scan spectrum shown in Fig. 5(a) indicates the presence of Zn, S, Ce, C and O elements in the synthesized samples. The carbon peak emanates from the adventitious carbon on the sample surface [28]. The O 1s spectra are assigned well to the peaks at 538 and 498.28 eV for ZnS and Ce doped ZnS mostly ascribed to

the chemisorbed  $H_2O$  or  $OH^-$  on the surface of the samples [29]. The binding energies for pure ZnS are 1049.64, 1026.65 and 1075 eV observed for Zn  $2p_{1/2}$ , Zn  $2p_{3/2}$  and Zn 2S respectively, which corresponds to  $Zn^{2+}$  according to the previous results [2,28,30]. Whereas for Ce doped ZnS the binding energy values were obtained at 1044.95 and 1022.05 eV for Zn  $2p_{1/2}$  and Zn  $2p_{3/2}$ , respectively. Owing to the doping effect, the binding energy values shifted to a lower energy. This is also assigned to the occurrence of some S vacancies [31]. From the spectra of Zn 2p in Fig. 5(b), the spin-orbit splitting between Zn  $2p_{3/2}$  and Zn  $2p_{1/2}$  is estimated to be 22.99, 22.9 eV for pure and Ce doped ZnS, which suggests the existence of  $Zn^{2+}$ . Figure 5(c) depicts the binding energies of S 2p and S 2s peaks for pure ZnS centered at 169, 176.4 and 249 eV, which are characteristic values of metal sulphide ( $S^{2-}$ ) species. Figure 5(d) shows high-resolution XPS spectra of Zn 3d, Zn 3p, and Zn 3s. The binding energies belong to  $S^{2-}$ ,  $2p_{3/2}$ ,  $2p_{1/2}$  and 2s, respectively in zinc–sulfur bond nanoparticles [32]. The decreasing binding energy of Ce doped sample attributes to the replacement of  $Ce^{3+}$  by  $Zn^{2+}$ . The Ce 3d spectra of Ce doped ZnS nanorods prepared with 5 wt.% precursor are shown in Fig. 5(a). It exhibits four peaks in the range of 885–917 eV. The peaks appear at 885.6 and 917 eV matched to  $Ce^{4+}$ . The peaks at 895 and 904.5 eV indicate that Ce ion has a +3 oxidation valance state [33] with Ce  $3d_{5/2}$  state. The

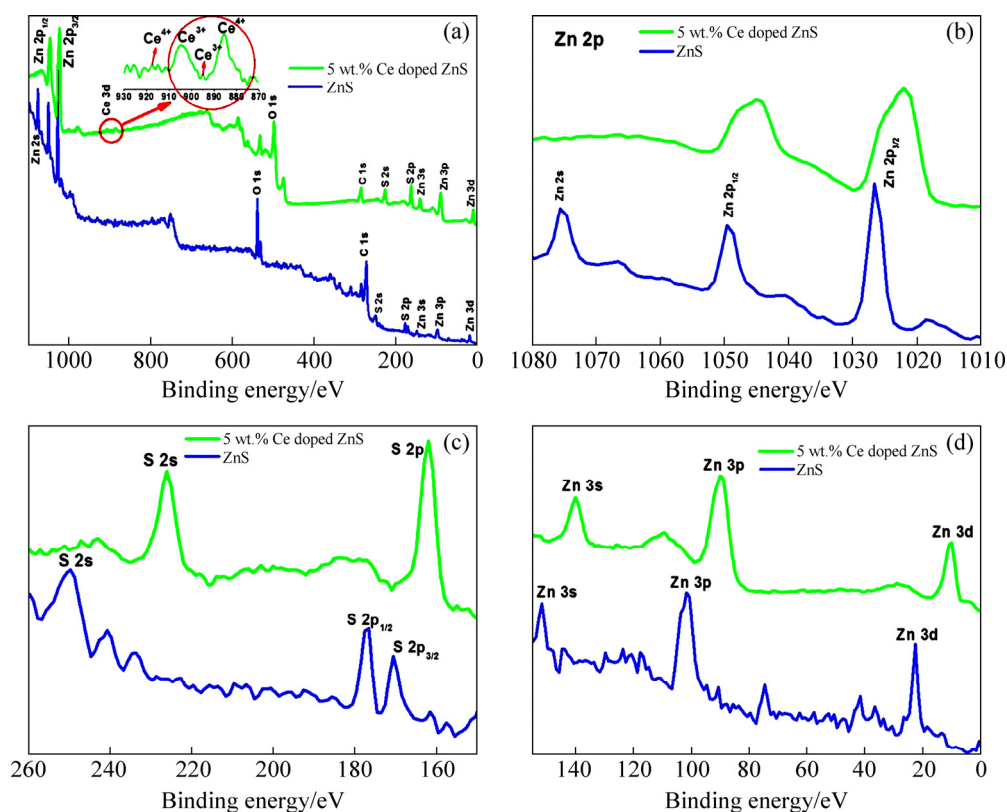


**Fig. 5** XPS analyses of full survey of ZnS (a), Zn 2p (b), S 2p (c) and Zn 3d, Zn 3p, Zn 3s (d)

binding energy of 895 eV is associated with Ce 3d<sub>5/2</sub> state, signifying spin-orbit coupling of Ce 3d<sub>5/2</sub> and Ce 3d<sub>3/2</sub> states. Furthermore, the peaks at 904.5 and 917 eV refer to the Ce 3d<sub>3/2</sub> state [34]. The XPS spectra of Ce 3d (Fig. 5(a)) indicated the presence of a mixed oxidation states (Ce<sup>3+</sup> and Ce<sup>4+</sup>) in the Ce doped ZnS in which f electron states are partially occupied or empty [33].

### 3.5 Raman studies

Raman measurements were carried out to understand the defect and structure of the samples. The first and second-order Raman spectra of ZnS:Ce (5 wt.%) are shown in Fig. 6. The 5 wt.% Ce doped ZnS nanorod samples have a strong peak at 72.7 cm<sup>-1</sup> and other peaks appear at 55.8, 169, 251, 343.7, 420, 498, 575, 620 and 670 cm<sup>-1</sup> and their first-order spectra of transverse-optical (TO) and longitudinal optical (LO) modes are located at 251 and 343.7 cm<sup>-1</sup>. Moreover, Ce doped ZnS belongs to the wurtzite structure of the symmetric space group C<sub>6v</sub>(P6<sub>3</sub>mc) in the primitive cell. The zone-centre optical phonon can be classified as the following irreducible representation:

$$\Gamma_{\text{opt}} = A_1 + E_1 + 2E_2 + 2B_1 \quad (1)$$

The B<sub>1</sub> modes are silent modes. In Eq. (1), A<sub>1</sub> and E<sub>1</sub> modes are polar modes and each splits into TO and LO components and both are Raman and infrared active. E<sub>2</sub> modes are nonpolar and Raman active and only have two frequencies, the higher-frequency E<sub>2</sub> (high) mode is associated with the sulphur atoms and the lower-frequency E<sub>2</sub> (low) mode is associated with the vibration of the heavy Zn sublattice. The B<sub>1</sub> modes are silent modes. The peak at 251 cm<sup>-1</sup> is due to the polar nature of the wurtzite ZnS. Hence, the peak at 251 cm<sup>-1</sup> observed in the present samples can be tentatively attributed to the LO phonon-plasmon coupled (LOPC) L<sup>-</sup> mode [31]. It might be the formation of a small portion of the intermediate state due to the incomplete conversion during the synthesis process [35]. The modes A<sub>1</sub> (TO) and E<sub>1</sub> (TO) occur at the wave number of 275 and 288 cm<sup>-1</sup>, respectively. The peak observed around 296 cm<sup>-1</sup> corresponds to E<sub>2</sub><sup>2</sup> and confirms that the structure is wurtzite type [36]. Other peaks appeared at 72 cm<sup>-1</sup> as E<sub>2</sub><sup>1</sup>, which is associated with the vibration of the heavy Zn sublattice. The optical phonon mode A<sub>1</sub> (LO)=E<sub>1</sub> (LO) is observed at 347 cm<sup>-1</sup>. The relative intensity of this peak is a measurement of the concentration of crystalline defects in the system. Compared to the Raman spectrum of bulk hexagonal ZnS (TO: 274 cm<sup>-1</sup> and LO: 352 cm<sup>-1</sup>), the peaks of the first-order LO and TO phonons shifted towards the lower energy.

Additionally, the Raman line of Ce doped sample reveals significant broadening. Such a phonon softening

and line broadening of the Raman peaks can be related to quantum confinement effects [37]. This might be due to small amount of compressive strain, large number of sulfur (S) vacancies and the ionic radius of Ce<sup>3+</sup> being higher than that of Zn<sup>2+</sup> [38]. Owing to resonant processes in the high-energy region (420–671 cm<sup>-1</sup>) second-order TO and LO phonons are observed. Further, Raman modes corresponding to other impurities are not observed. An additional peak located at 55.8 cm<sup>-1</sup> is the characteristic Raman scattering of ZnS and indexed to [LO-TO] phonon mode [39]. The reported frequencies of the Raman active modes of wurtzite Ce doped ZnS are shown in Table 2. Thus, the defect is arising from the sulphur vacancy.

**Table 2** First-order Raman frequencies of hexagonal wurtzite 5 wt.% Ce doped ZnS

Order	Raman shift/cm <sup>-1</sup>		Assignment
	Present study	Ref.	
First order	Not observed	110 [40]	LA
	147	139 [35]	2TA
	218	216 [37] 219 [41]	LA
	251	251 [31]	LOPC
	72	72 [42]	E <sub>2</sub> <sup>1</sup>
	275	275 [36]	A <sub>1</sub> (TO)
	288	288 [36]	E <sub>1</sub> (TO)
	296	296 [36]	E <sub>2</sub> <sup>2</sup>
	347	347 [36]	A <sub>1</sub> (LO)/E <sub>1</sub> (LO)
Second order	420	422 [31]	LO+TA
	619	615 [43] 617 [44]	2TO
	642	642 [44]	TO+LA
	671	673 [44]	2LO

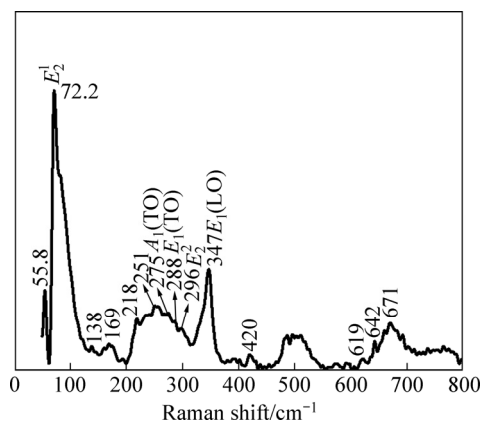


**Fig. 6** Room temperature Raman spectrum of 5 wt.% Ce doped ZnS nanorods

### 3.6 Optical studies

The typical diffuse reflectance spectra of ZnS:Ce is shown in Fig. 7. The reflectance values of ZnS:Ce (0, 3 and 5 wt.%) are 78.4%–15%, 90.1%–21.5% and 79%–9.2%, respectively. Figure 7 reveals that 3 wt.% Ce doping has the maximum reflectance (90.1%–21.5%) because the  $Ce^{3+}$  ions incorporated at  $Zn^{2+}$  sites might be covalently bonded to ZnS [28]. However, with increasing Ce content there is an obvious decrease in reflectance in samples of higher dopant concentrations. This decrease may be a result of light being scattered by grain boundaries as well as Ce clusters [27]. The bandgap of the sample is estimated by Kubelka–Munk method. Optical band gap from reflectance spectra for undoped and Ce doped samples is illustrated in the inset of Fig. 7. The values of bandgap energy obtained for undoped and Ce doped ZnS are 3.50, 3.405 and 3.38 eV, respectively. It is clear that the bandgap energy is blue shifted from the bulk ZnS (3.68 eV), which could be caused by the quantum confinement effect.

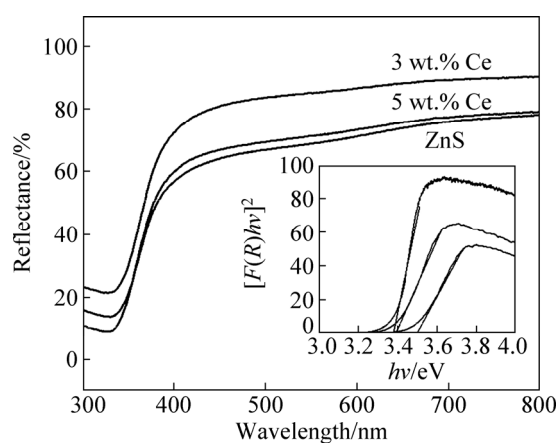


**Fig. 7** Diffuse reflectance spectra of ZnS:Ce and their inset diagram showing bandgap calculation

### 3.7 Magnetic properties

The  $M-H$  curves for ZnS, 3% and 5 wt.% Ce doped ZnS are presented in Figs. 8(a–c). The magnetization as a function of the external field is described by a hysteresis curve. The  $M-H$  curve indicates that the entire samples exhibit ferromagnetism. The hysteresis loops with magnetization  $M_s=0.02924 \text{ A}\cdot\text{m}^2/\text{kg}$  are observed for the undoped ZnS nanoparticles and 3 wt.% and 5 wt.% Ce-doped samples exhibit  $M_s=0.01492$  and  $0.01382 \text{ A}\cdot\text{m}^2/\text{kg}$  and their coercivity values are 93.43,  $590.28 \times 10^{-4}$  and  $471 \times 10^{-4} \text{ T}$ .

Normally, the origin of ferromagnetic property in DMS can be understood from three conditions: second phase related to rare-earth sulphide; rare-earth clusters; intrinsic effect of DMS. In our study, we suspect the origin of the observed ferromagnetic order in the ZnS nanoparticles by the intrinsic effect. Figure 8(a) shows

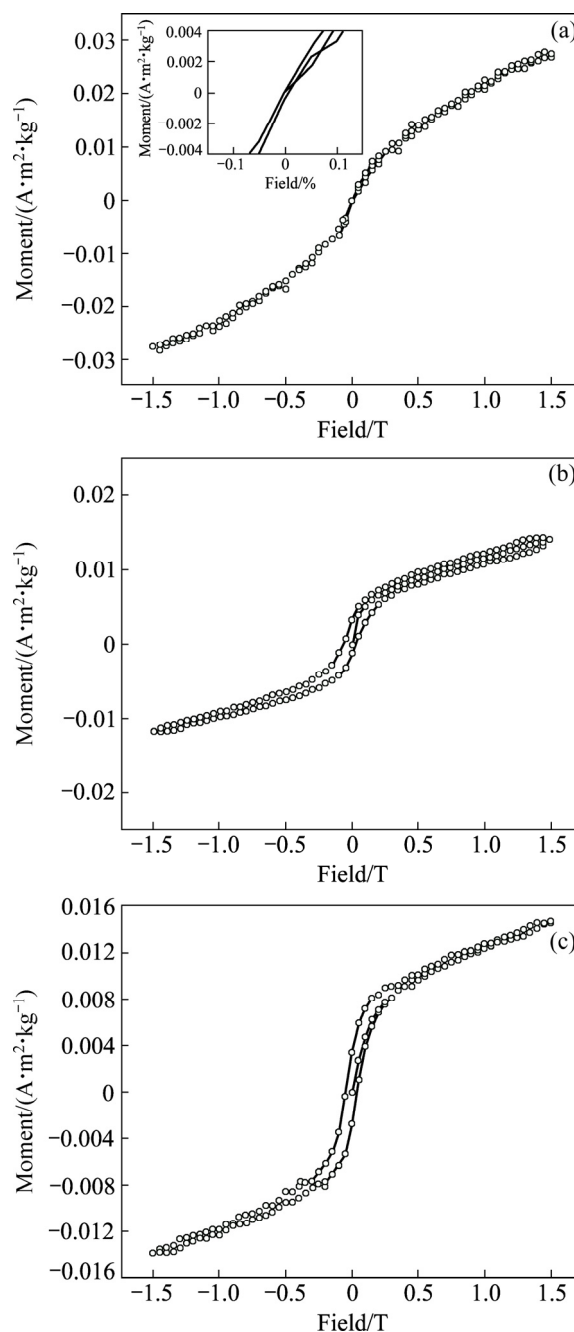


**Fig. 8** Hysteresis loop measured at 300 K for ZnS:Ce: (a) 0 wt.% Ce; (b) 3 wt.% Ce; (c) 5 wt.% Ce

that the hysteresis loops of undoped ZnS have weak ferromagnetic nature. According to Hund's rule, an atom in which the electron levels are partially filled, the magnetic moment will be due to the total angular momentum. In most solids the average value of total angular momentum  $\langle L_z \rangle_{\text{avg}}=0$ , i.e.  $L_z$  in the solid is quenched. Thus, the permanent magnetic moment in most of the solids occurred by the spin angular momentum only. Magnetic moment arises in ferromagnetic material due to the partially filled d and f shells. In ZnS,  $Zn^{2+}$  ions have 3d filled states. Owing to annealing, an increase in kinetic energy of the electrons

in 3d shell of  $\text{Zn}^{2+}$  ions gives rise to a small magnetic moment per atom. This increase in kinetic energy is a result of the exchange interaction between  $\text{Zn}^{2+}$  ions and  $\text{S}^{2-}$  ions.

The exchange integral ( $j_{ij}$ ) depends on the interatomic distance ( $R$ ). The exchange integral is positive for  $R > 1.5 \text{ \AA}$  and negative for  $R < 1.5 \text{ \AA}$ . The  $R$  of zinc blende is  $2.36 \text{ \AA}$  and that of wurtzite is  $2.35 \text{ \AA}$ . On account of, tetrahedral arrangement of zinc blende each zinc atom has 4 sulphur atoms in its first coordination sphere and 12 atoms in its own type in the second coordination sphere [45]. Moreover, the atomic distance of zinc blende is  $> 1.5 \text{ \AA}$  due to its structure and strong electro negativity of ZnS which leads to small magnetic moment. The exchange interaction between  $\text{Zn}^{2+}$  and  $\text{S}^{2-}$  ions in effect with sulphur vacancy exhibits ferromagnetism in the magnetic field. Room temperature ferromagnetism of nanowire arising from unpaired 3p electrons at S sites surrounding the Zn vacancies carrying the magnetic moment [46] and  $d^0$  ferromagnetism in undoped ZnS nanoparticles due to sulphur vacancy [6] has been studied.

The origin of the ferromagnetic coupling in rare earth metals doped semiconductor is also a topic of great interest. It is apparent that strong ferromagnetic coupling is not a result of direct exchange interaction of Heisenberg because there is a lack of overlap between neighbouring 4f shells. This contradiction could be resolved by the indirect exchange coupling via conduction electrons. The long-range nature of the indirect exchange coupling may cause the peculiar magnetic properties of the rare-earth ion [47,48]. Since 4f electrons are localized in Ce, the exchange interaction is not direct along 5d or 6s electrons and directing high total angular momentum. 4f electrons in Ce ion are shielded from the crystalline field by outer 5d and 6s shells and the neighbouring ligands have very little effect on the 4f electrons. On account of the weak interaction with lattice environment, the energy levels of the 4f electrons are very similar to free ion levels characterized by  $L$ ,  $S$  and  $J$  values. This weak interaction also leads to magnetic coupling strength of f orbitals and weaker than d orbitals.

The electronic configuration of Ce atom is  $4f^1 5d^1 6s^2$ . Since the interaction along 4f–5d is swap, it is decided that the observed ferromagnetism in Ce doped sample might be due to indirect exchange coupling via conduction electrons by inter-ion 5d–5d coupling [20]. As the Ce concentration increases the coercive field ( $H_c$ ) and magnetization ( $M_s$ ) are in diminishing trend.

The soft ferromagnetic properties have been observed in 5 wt.% Ce doped ZnS nanorods in Fig. 8(c). It was found that a uniaxial magnetic anisotropy was induced along (102) direction instead of (111) direction

of cubic structure, under an applied magnetic field. The soft phases in a Ce doped sample should be perfectly exchanged and coupled for the coherent rotation of the magnetization. In the case of poor exchange-coupling or no coupling, the soft phase magnetization rotates with the magnetic field freely. The magnetization ( $M_s$ ) of 5 wt.% Ce doped sample decreases compared to lower doping concentration. This may be due to antiferromagnetism between the nearest neighbour Ce–Ce ions [49]. Many research groups have claimed to observe ferromagnetic behaviour arising only from dopant impurity phases [50]. Therefore, it is inferred that the RT weak ferromagnetism for undoped ZnS could be related to the defects. However, as synthesized ZnS NPs are diamagnetic, which has been reported in our previous work [51]. There is no magnetic report on Ce doped ZnS of any form for comparison. However, in a similar system (ZnS:Gd) and (ZnS:Nd) such decreased magnetism with increasing dopant content has been observed [19,27].

## 4 Conclusions

(1) In summary, aimed at finding ferromagnetism at room temperature, ZnS:Ce samples were synthesized by co-precipitation method using PEG as a capping agent. 5 wt.% Ce doped ZnS nanorods have soft ferromagnetism compared to undoped ZnS nanoparticles.

(2) High resolution XPS spectra provided the evidence for Zn–S bonding and the presence of a mixed valence state ( $\text{Ce}^{3+}$  and  $\text{Ce}^{4+}$ ) in the 5 wt.% Ce doped ZnS nanorods.

(3) A crucial role of the sulphur defects is confirmed by Raman results. The thermal analysis of Ce doped nanorods confirms that the synthesized sample has high thermal stability and decomposition temperature.

(4) The average diameter of the nanoparticles and rod-like shape are probed by TEM image. Structural analysis indicates that the Ce doped ZnS is hexagonal phase. The reflectance spectra and EDAX validate the incorporation of  $\text{Ce}^{3+}$  into ZnS.

(5) Nanoscale effects on spin structure of magnetic materials like ZnS:Ce nanorods may help to provide a pathway for developing technologies pertinent to spintronic and other devices.

## Acknowledgments

The authors would like to thank SAIF, IIT (M)-Chennai for providing VSM facility to carry out this research work successfully.

## References

- [1] ANDREW F, VICTOR I R, XAVIER F, MARIA I, ANDREU C,

- EDGARDO S, ALEJANDRO P R. ZnS grain size effects on near-resonant Raman scattering: Optical non-destructive grain size estimation [J]. *Crystal Eng Comm*, 2014, 16: 4120–4125.
- [2] GAO Da-qiang, YANG Gui-jin, ZHANG Jing, ZHU Zhong-hua, SI Ming-su, XUE De-sheng. d<sub>0</sub> ferromagnetism in undoped sphalerite ZnS nanoparticles [J]. *Applied Physics Letters*, 2011, 99: 052502.
- [3] BALCELLS L L, BELTRAN, J I, MARTINEZ-BOUBETA C, KONSTANTINOVIC Z, ARBIOL J, MARTINEZ B. Aging of magnetic properties in MgO films [J]. *Applied Physics Letters*, 2010, 97: 252503.
- [4] MONIKA M, PANKAJ K, CHAND S, LOKENDRA K. Influence of ZnS quantum dots on optical and photovoltaic properties of poly (3-hexylthiophene) [J]. *Chemical Physics Letters*, 2010, 495: 236–240.
- [5] TSURUOKA T, LIANG C H, TERABE K, HASEGAWA T. Origin of green emission from ZnS nanobelts as revealed by scanning near-field optical microscopy [J]. *Applied Physics Letters*, 2008, 92: 091908.
- [6] ZHU Guo-xing, ZHANG Shu-guang, XU Zheng, MA Jing, SHEN Xiao-ping. Ultrathin ZnS single crystal nanowires: Controlled synthesis and room-temperature ferromagnetism properties [J]. *Journal of the American Chemical Society*, 2011, 133: 15605–15612.
- [7] WANG Gang, HUANG Bai-biao, LI Zhu-jie, LOU Zai-zhu, WANG Ze-yan, DAI Ying, WHANGBO M H. Synthesis and characterization of ZnS with controlled amount of S vacancies for photocatalytic H<sub>2</sub> production under visible light [J]. *Scientific Reports*, 2015, 5: 8544.
- [8] VITALY P, SABIT H, JINKE T, YURI D. Room temperature d<sup>0</sup> ferromagnetism in ZnS nanocrystals [J]. *Journal of Applied Physics*, 2016, 119: 223901.
- [9] PRADHAN N, PENG X. Efficient and color-tunable Mn-doped ZnSe nanocrystal emitters: Control of optical performance via greener synthetic chemistry [J]. *Journal of the American Chemical Society*, 2007, 129: 3339–3347.
- [10] REMI B, PAUL I A, STEFAN T O, DANIEL R G. Mn<sup>2+</sup>-doped CdSe quantum dots: New inorganic materials for spin-electronics and spin-photonics [J]. *Advanced Functional Materials*, 2008, 18: 3873–3891.
- [11] SANJEEV K, CHEN C L, DONG C L, HO Y K, LEE J F, CHAN T S, THANGAVEL R, CHEN T K, MOK B H, RAO S M, WU M K. Room temperature ferromagnetism in Ni doped ZnS nanoparticles [J]. *Journal of Alloys and Compounds*, 2013, 554: 357–362.
- [12] van VLECK J H. The theory of electric and magnetic susceptibilities [M]. London: Oxford University Press, 1932.
- [13] NIIRA K. Temperature dependence of the magnetization of dysprosium metal [J]. *Physical Review*, 1960, 117: 129–133.
- [14] ZHOU Dan-jie, XIE Xin-yuan, ZHANG Yan-li, GUO Dan-yi, ZHOU Yi-jia, XIE Jin-feng. Facile synthesis of ZnS nanorods in PEG and their spectral performance [J]. *Materials Research Express*, 2016, 3: 105023.
- [15] ZHAO Wen-hua, WEI Zhi-qiang, ZHANG Li, WU Xiao-juan, WANG Xuan, JIANG Jin-long. Room temperature ferromagnetic and optical properties of chrome doped ZnS nanorods prepared by hydrothermal method [J]. *Journal of Nanomaterials*, 2017, <https://doi.org/10.1155/2017/9378349>.
- [16] CHEN Yun, YIN Rong-hui, WU Qing-sheng. Solvothermal synthesis of well-disperse ZnS nanorods with efficient photocatalytic properties [J]. *Journal of Nanomaterials*, 2012, <http://dx.doi.org/10.1155/2012/560310>.
- [17] SABIT H, BAICHHABI Y, UMA P, JON M P, WANG Wen-yong, TANG Jin-ke. Controlled synthesis of Eu<sup>2+</sup> and Eu<sup>3+</sup> doped ZnS quantum dots and their photovoltaic and magnetic properties [J]. *AIP Advances*, 2016, 6: 045119.
- [18] POORNAPRAKASH B, CHALAPATHI U, MADDAKA R, SI-HYUN P. Effect of Gd doping on the structural, luminescence and magnetic properties of ZnS nanoparticles synthesized by the hydrothermal method [J]. *Superlattices and Microstructures*, 2016, 97: 104–110.
- [19] DHIRENDRA KUMAR S, KAPIL KUMAR S, VIPIN K, ANURADHA S. Effect of Ce doping on the structural, optical and magnetic properties of ZnO nanoparticles [J]. *Journal of Materials Science: Materials in Electronics*, 2016, 27: 10330–10335.
- [20] BRIAN M W. Judd-ofelt theory: Principles and practices [M]. Netherlands: Springer, 2005: 403–433.
- [21] TANG R, SU H, DUAN S, SUN Y, LI L, ZHANG X, ZENG S, SUN D. Enhanced visible-light-driven photocatalytic performances using Bi<sub>2</sub>WO<sub>6</sub>/MS (M=Cd, Zn) heterostructures: facile synthesis and photocatalytic mechanisms [J]. *RSC Advances*, 2015, 5: 41949–41960.
- [22] RAMESH S, WANG K C. Conductivity, dielectric behavior and thermal stability studies of lithium ion dissociation in poly (methyl methacrylate)-based gel polymer electrolytes [J]. *Ionics*, 2009, 15: 249–254.
- [23] SHE Y Y, YANG J, QIU K Q. Synthesis of ZnS nanoparticles by solid-liquid chemical reaction with ZnO and Na<sub>2</sub>S under ultrasonic [J]. *Transactions of Nonferrous Metals Society of China*, 2010, 20(S1): s211–s215.
- [24] SHANMUGAM N, CHOLAN S, VIRUTHAGIR G, GOBI R, KANNADASAN N. Synthesis and characterization of Ce<sup>3+</sup>-doped flowerlike ZnS nanorods [J]. *Applied Nanoscience*, 2014, 4: 359–365.
- [25] RAMU S, VIJAYALAKSHMI R P. Effect of terbium doping on the structural and magnetic properties of ZnS nanoparticles [J]. *Journal of Superconductivity and Novel Magnetism*, 2017, 30:1921–1925.
- [26] ZEEN V O, ALAEDDIN A S, YUFRIDIN W, ZUL AZHAR Z J. X-ray line profile analysis of BaTiO<sub>3</sub> thin film prepared by sol-gel deposition [J]. *American Institute of Physics Conference Series*, 2017, 1835: 020011.
- [27] RAM K, ATUL K G, SHEO K M, RAJNEESH K S, AVINASH C P, PRAKASH S G. Photoluminescence and photoconductivity of ZnS: Mn (2+) nanoparticles synthesized via co-precipitation method [J]. *Spectrochimica Acta (Part A)*, 2010, 76: 523–527.
- [28] DI B B, FORTE O. Advances in spectroscopy for lasers and sensing [M]. Springer, 2005: 403–433.
- [29] YANG Xia, XUE Hong-tao, XU Jun, HUANG Xing, ZHANG Jie, TANG Yong-bing, NG Tsz-wai, KWONG Hoi-lun, MENG Xiang-min, LEE Chun-sing. Synthesis of porous ZnS: Ag<sub>2</sub>S nanosheets by ion exchange for photocatalytic H<sub>2</sub> generation [J]. *ACS Applied Materials & Interfaces*, 2014, 6: 9078–9084.
- [30] ZHANG Hai-lin, WEI Bo, ZHU Lin, YU Jia-hui, SUN Wen-jun, XU Ling-ling. Cation exchange synthesis of ZnS–Ag<sub>2</sub>S microspheric composites with enhanced photocatalytic activity [J]. *Applied Surface Science*, 2013, 270:133–138.
- [31] GAWAI U P, DESHPANDE U P, DOLE B N. A study on the synthesis, longitudinal optical phonon-plasmon coupling and electronic structure of Al doped ZnS nanorods [J]. *RSC Advances*, 2017, 7: 12382–12390.
- [32] KALYANARAMAN K, VAITHILINGAM S. Photodegradation and antibacterial studies of ZnS enwrapped fly ash nanocomposite for multipurpose industrial applications [J]. *RSC Advances*, 2015, 5: 47766–47777.
- [33] CHANG Chi-jung, HUANG Kuo-lin, CHEN Jem-kun, CHU Kuan-wu, HSU Mu-hsiang. Improved photocatalytic hydrogen production of ZnO/ZnS based photocatalysts by Ce doping [J]. *Journal of the Taiwan Institute of Chemical Engineers*, 2015, 55: 82–89.

- [34] NABANITA P, INDRANI M, SRIPARNA C, CHO Eun-bum. Surfactant-assisted synthesis of ceria–titania-rich mesoporous silica materials and their catalytic activity towards photodegradation of organic dyes [J]. Dalton Transactions, 2017, 46: 9577–9590.
- [35] ZHANG H, CHEN Q, ZHANG H, RUI W, DING Q, CAO Y, ZHONG W, SHEN K, DU J, XIANG D, XU Q. Interstitial H<sup>+</sup>-mediated ferromagnetism in Co-doped ZnS [J]. Journal of Superconductivity and Novel Magnetism, 2015, 28: 1389–1393.
- [36] CHENG Y C, JIN C Q, GAO F, WU X L, ZHONG W, LI S H, CHU P K. Raman scattering study of zinc blende and wurtzite ZnS [J]. Journal of Applied Physics, 2010, 106: 123505.
- [37] NILSEN W G. Raman spectrum of cubic ZnS [J]. Physical Review, 1969, 182: 838–850.
- [38] RICHARD D YANG, TRIPATHY S, FRANCIS E H T, GAN L M, CHUA S J. Photoluminescence and micro-Raman scattering in Mn-doped ZnS nanocrystalline semiconductors [J]. Journal of Vacuum Science & Technology B, 2003, 21: 984–988.
- [39] TALWAR D N, AGRAWAL B K. Raman spectrum of cubic zinc sulphide—An interpretation [J]. Phys Stat Sol (b), 1974, 64: 71–78.
- [40] SARAVANAN KUMAR S, ABDUL KHADAR M, DHARA S K, RAVINDRAN T R, NAIR K G M. Photoluminescence and Raman studies of ZnS nanoparticles implanted with Cu<sup>+</sup> ions [J]. Nuclear Instruments and Methods in Physics Research Section B, 2006, 251: 435–440.
- [41] LU H, CHU S, CHANG C. Synthesis and optical properties of well-aligned ZnS nanowires on Si substrate [J]. Journal of Crystal Growth, 2005, 280: 173–178.
- [42] BRAFMAN O, MITRA S S. Raman effect in wurtzite- and zinc-blende-type ZnS single crystals [J]. Physical Review, 1968, 171: 931–933.
- [43] SUGANTHI N, PUSHPANATHAN K. Paramagnetic nature of Mn doped ZnS nano particles in opto electronic device application [J]. Journal of Materials Science: Materials in Electronics, 2016, 27: 10089–10098.
- [44] POORNAPRAKASH B, NAVEEN KUMAR K, CHALAPATHI U, REDDEPPA M, POOJITHA P T, SI-HYUN P. Chromium doped ZnS nanoparticles: Chemical, structural, luminescence and magnetic studies [J]. Journal of Materials Science: Materials in Electronics, 2016, 27: 6474–6479.
- [45] AMARANATHA REDDY D, MURALI G, POORNAPRAKASH B, VIJAYALAKSHMI R P, REDDY B K. Structural, optical and magnetic properties of Zn<sub>0.97- $\alpha$</sub> Cu <sub>$\alpha$</sub> Cr<sub>0.03</sub>S nanoparticles [J]. Applied Surface Science, 2012, 258: 5206–5211.
- [46] MUKESH J. Diluted magnetic semiconductor [M]. Singapore: World Scientific Publishing Co. Pvt. Ltd, 1991: 7–10.
- [47] KASUYA T. Electrical resistance of ferromagnetic metals [J]. Progress of Theoretical Physics, 1956, 16: 58–63.
- [48] ZENER C. Interaction between the d shells in the transition metals [J]. Physical Review, 1951, 81: 440–444.
- [49] ZENER C, HEIKES R R. Exchange interaction [J]. Review of Modern Physics, 1953, 25: 191–198.
- [50] PALVINDER K, SANJEEV K, ANUPINDER S, CHEN C L, DONG C L, CHAN T S, LEE K P, SRIVASTAVA C, RAO S M, WU M K. Investigations on doping induced changes in structural, electronic structure and magnetic behavior of spintronic Cr–ZnS nanoparticles [J]. Superlattices and Microstructures, 2015, 83: 785–795.
- [51] OMRIO K, LEMINE O M, GHOUL J E, MIR L E. Sol–gel synthesis and room temperature ferromagnetism in Mn doped ZnO nanocrystals [J]. Journal of Materials Science: Materials in Electronics, 2015, 26: 5930–5936.

## 铈掺杂 ZnS 纳米棒中相变对室温铁磁性的影响

Nachimuthu SUGANTHI, Kuppusamy PUSHPANATHAN

Nanomaterials Research Laboratory, Department of Physics, Government Arts College, Karur-639 005, India

**摘要:** 研究铈掺杂对化学共沉淀法合成的 ZnS:Ce 纳米棒的结构、光学性能、氧化性能、热性能和磁性能的影响。结果显示, 铈掺杂后, ZnS 晶体结构由立方结构转变为六方结构。磁性能检测结果表明, 掺铈 ZnS 纳米棒具有室温铁磁性。X 射线光电子能谱(XPS)结果证明其近表面区域存在 Zn–S 键和氧化态的铈。拉曼光谱结果表明, 掺 5 wt.% Ce 的 ZnS 纳米棒为六方结构, 且存在缺陷。利用透射电镜(TEM)研究铈取代诱导的形状演变。DRS 光谱进一步证实了 Ce<sup>3+</sup>离子的掺入。本研究揭示铈掺杂的 ZnS 纳米棒可能在自旋电子器件方面有应用前景。

**关键词:** 铈掺杂; ZnS 纳米棒; 相变; 铁磁性; 硫空位; 热稳定性

(Edited by Xiang-qun LI)